$$\mathrm{Im}\left(-\frac{1}{\sum_i \varepsilon_{ii} q_i^2}\right). \qquad (4.3.4.28)$$

In a uniaxial crystal, such as a graphite, $\varepsilon_{11} = \varepsilon_{22} = \varepsilon_\perp$ and $\varepsilon_{33} = \varepsilon_\parallel$ (*i.e.* parallel to the c axis):

$$\varepsilon(\mathbf{q}, \omega) = \varepsilon_\perp \sin^2\theta + \varepsilon_\parallel \cos^2\theta, \qquad (4.3.4.29)$$

where θ is the angle between $\mathbf{q}$ and the c axis. The spectrum depends on the direction of $\mathbf{q}$, either parallel or perpendicular to the c axis, as shown in Fig. 4.3.4.19 from Venghaus (1975). These experimental conditions may be achieved by tilting the graphite layer at 45° with respect to the incident axis, and recording spectra in two directions at $\pm\theta_E$ with respect to it (see Fig. 4.3.4.20).

4.3.4.3.4. *Surface plasmons*

Volume plasmons are longitudinal waves of charge density propagating through the bulk of the solid. Similarly, three exist longitudinal waves of charge density travelling along the surface between two media A and B (one may be a vacuum): these are the surface plasmons (Kliewer & Fuchs, 1974). Boundary conditions imply that

$$\varepsilon_A(\omega) + \varepsilon_B(\omega) = 0. \qquad (4.3.4.30)$$

The corresponding charge-density fluctuation is contained within the (**x**) boundary plane, z being normal to the surface:

$$\rho(\mathbf{x}, z) \simeq \cos(\mathbf{q}\cdot\mathbf{x} - \omega t)\delta(z), \qquad (4.3.4.31)$$

and the associated electrostatic potential oscillates in space and time as

$$\varphi(\mathbf{x}, z)\, \alpha \cos(\mathbf{q}\cdot\mathbf{x} - \omega t)\exp(-q|z|). \qquad (4.3.4.32)$$

The characteristic energy ω_s of this surface mode is estimated in the free electron case as:

In the planar interface case:

$$\left.\begin{aligned}
&\omega_s = \frac{\omega_p}{\sqrt{2}} \\
&\quad \text{(interface metal–vacuum);} \\
&\omega_s = \frac{\omega_p}{(1+\varepsilon_d)^{1/2}} \\
&\quad \text{(interface metal–dielectric of constant } \varepsilon_d\text{);} \\
&\omega_s = \left(\frac{\omega_{p_A}^2 + \omega_{p_B}^2}{2}\right)^{1/2} \\
&\quad \text{(interface metal } A\text{–metal } B\text{).}
\end{aligned}\right\} \qquad (4.3.4.33)$$

In the spherical interface case:

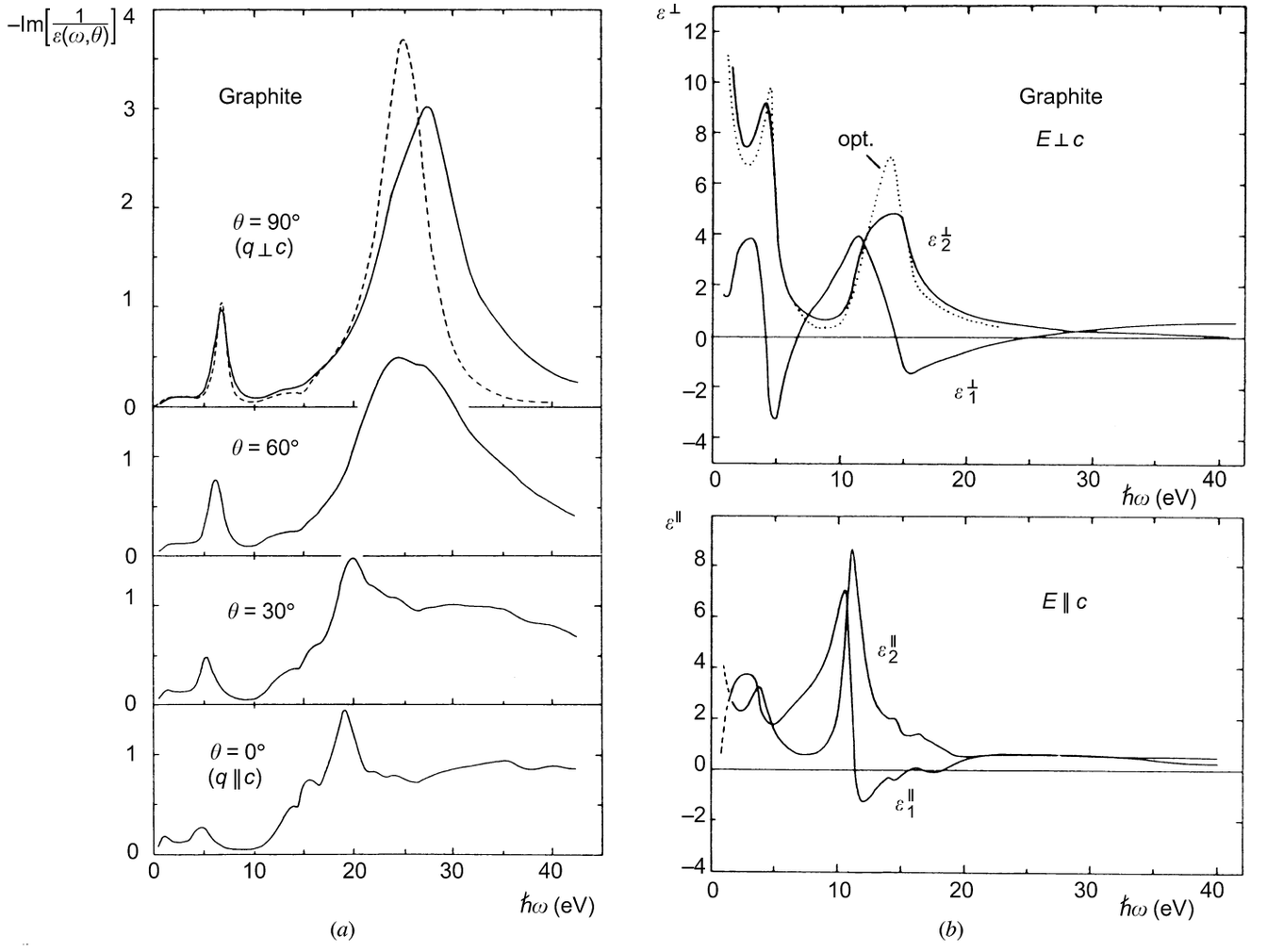

Fig. 4.3.4.19. Dielectic functions in graphite derived from energy losses for $E \perp c$ (*i.e.* the electric field vector being in the layer plane) and for $E \| c$ [from Daniels *et al.* (1970)]. The dashed line represents data extracted from optical reflectivity measurements [from Taft & Philipp (1965)].

$$(\omega_s)_l = \frac{\omega_p}{[(2l+1)/l]^{1/2}} \qquad (4.3.4.34a)$$

(metal sphere in vacuum – the modes are now quantified following the l quantum number in spherical geometry);

$$(\omega_s)_l = \frac{\omega_p}{[(2l+1)/(l+1)]^{1/2}} \qquad (4.3.4.34b)$$

(spherical void within metal).

Thin-film geometry:

$$(\omega_s)^{\pm} = \omega_p \left[\frac{1 \pm \exp(-qt)}{1+\varepsilon_d}\right]^{1/2} \qquad (4.3.4.35)$$

(metal layer of thickness t embedded in dielectric films of constant ε_d). The two solutions result from the coupling of the oscillations on the two surfaces, the electric field being symmetric for the $(\omega_s)^-$ mode and antisymmetric for the $(\omega_s)^+$.

In a real solid, the surface plasmon modes are determined by the roots of the equation $\varepsilon(\omega_s) = -1$ for vacuum coating [or $\varepsilon(\omega_s) = -\varepsilon_d$ for dielectric coating].

The probability of surface-loss excitation P_s is mostly governed by the $\mathrm{Im}\{-1/[1+\varepsilon(\omega)]\}$ energy-loss function, which is analogous for surface modes to the bulk $\mathrm{Im}\{-1/[\varepsilon(\omega)]\}$ energy-loss function. In normal incidence, the differential scattering cross section $\mathrm{d}P_s/\mathrm{d}\Omega$ is zero in the forward direction, reaches a maximum for $\theta = \pm\theta_E/3^{1/2}$, and decreases as θ^{-3} at large angles. In non-normal incidence, the angular distribution is asymmetrical, goes through a zero value for momentum transfer $\hbar\mathbf{q}$ in a direction perpendicular to the interface, and the total probability increases as

$$P_s(\varphi) = \frac{P_s(O)}{\cos\varphi}, \qquad (4.3.4.36)$$

where φ is the incidence angle between the primary beam and the normal to the surface. As a consequence, the probability of producing one (and several) surface losses increases rapidly for grazing incidences.

4.3.4.4. *Excitation spectrum of core electrons*

4.3.4.4.1. *Definition and classification of core edges*

As for any core-electron spectroscopy, EELS spectroscopy at higher energy losses mostly deals with the excitation of well defined atomic electrons. When considering solid specimens, both initial and final states in the transition are actually eigenstates in the solid state. However, the initial wavefunction can be considered as purely atomic for core excitations. As a first consequence, one can classify these transitions as a function of the parameters of atomic physics: Z is the atomic number of the element; n, l, and $j = l + s$ are the quantum numbers describing the subshells from which the electron has been excited. The spectroscopy notation used is shown in Fig. 4.3.4.21. The list of major transitions is displayed as a function of Z and E_c in Fig. 4.3.4.22.

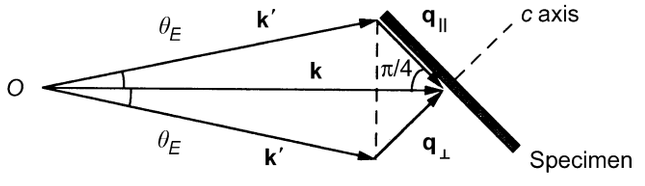

Fig. 4.3.4.20. Geometric conditions for investigating the anisotropic energy-loss function.

Core excitations appear as edges superimposed, from the threshold energy E_c upwards, above a regularly decreasing background. As explained below, the basic matrix element governing the probability of transition is similar for optical absorption spectroscopy and for small-angle-scattering EELS spectroscopy. Consequently, selection rules for dipole transitions define the dominant transitions to be observed, *i.e.*

$$l' - l = \Delta l = \pm 1 \quad \text{and} \quad j' - j = \Delta j = 0, \pm 1. \qquad (4.3.4.37)$$

This major rule has important consequences for the edge shapes to be observed: approximate behaviours are also shown in Fig. 4.3.4.22. A very useful library of core edges can be found in the EELS atlas (Ahn & Krivanek, 1982), from which we have selected the family of edges gathered in Fig. 4.3.4.23. They display the following typical profiles:

(i) *K edges for low-Z elements* ($3 \leq Z \leq 14$). The carbon K edge occurring at 284 eV is a nice example with a clear hydrogenic or saw-tooth profile and fine structures on threshold depending on the local environment (amorphous, graphite, diamond, organic molecules, ...); see Isaacson (1972*a*,*b*).

(ii) *$L_{2,3}$ edges for medium-Z elements* ($11 \lesssim Z \lesssim 45$). The $L_{2,3}$ edges exhibit different shapes when the outer occupied shell changes in nature: a delayed profile is observed as long as the first vacant d states are located, along the energy scale, rather above the Fermi level (sulfur case). When these d states coincide with the first accessible levels, sharp peaks, generally known as 'white lines', appear at threshold (this is the case for transition elements with the Fermi level inside the d band). These lines are generally split by the spin-orbit term on the initial level into $2p^{3/2}$ and $2p^{1/2}$ (or L_3 and L_2) terms. For higher-Z elements, the bound d levels are fully occupied, and

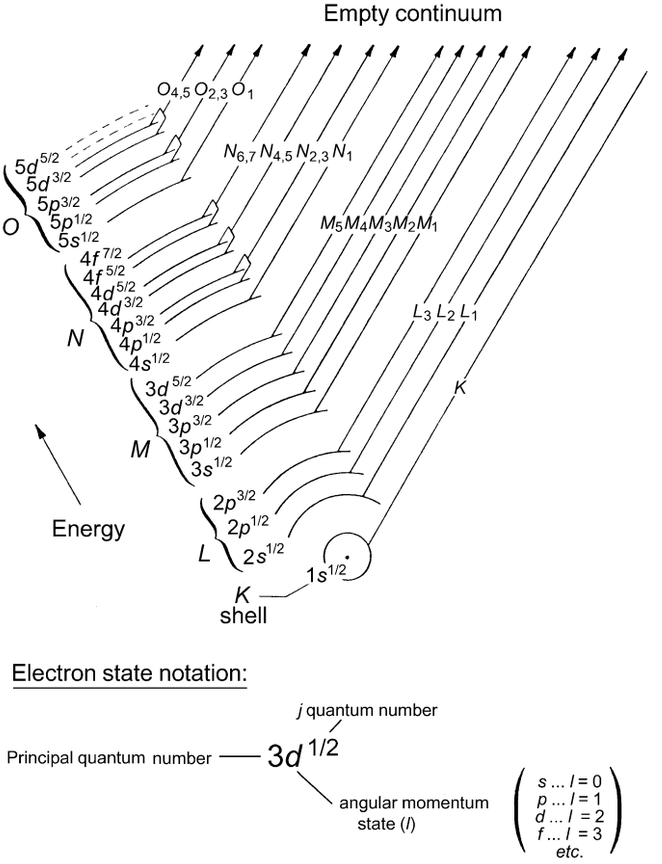

Fig. 4.3.4.21. Definition of electron shells and transitions involved in core-loss spectroscopy [from Ahn & Krivanek (1982)].

references